Latest Developments in SLD Scaling

Jen-Ching Tsao and David N. Anderson
Ohio Aerospace Institute, Cleveland, Ohio

NASA STI Program . . . in Profile

Since its founding, NASA has been dedicated to the advancement of aeronautics and space science. The NASA Scientific and Technical Information (STI) program plays a key part in helping NASA maintain this important role.

The NASA STI Program operates under the auspices of the Agency Chief Information Officer. It collects, organizes, provides for archiving, and disseminates NASA's STI. The NASA STI program provides access to the NASA Aeronautics and Space Database and its public interface, the NASA Technical Reports Server, thus providing one of the largest collections of aeronautical and space science STI in the world. Results are published in both non-NASA channels and by NASA in the NASA STI Report Series, which includes the following report types:

* TECHNICAL PUBLICATION. Reports of completed research or a major significant phase of research that present the results of NASA programs and include extensive data or theoretical analysis. Includes compilations of significant scientific and technical data and information deemed to be of continuing reference value. NASA counterpart of peer-reviewed formal professional papers but has less stringent limitations on manuscript length and extent of graphic presentations.

* TECHNICAL MEMORANDUM. Scientific and technical findings that are preliminary or of specialized interest, e.g., quick release reports, working papers, and bibliographies that contain minimal annotation. Does not contain extensive analysis.

* CONTRACTOR REPORT. Scientific and technical findings by NASA-sponsored contractors and grantees.

* CONFERENCE PUBLICATION. Collected papers from scientific and technical conferences, symposia, seminars, or other meetings sponsored or cosponsored by NASA.

* SPECIAL PUBLICATION. Scientific, technical, or historical information from NASA programs, projects, and missions, often concerned with subjects having substantial public interest.

* TECHNICAL TRANSLATION. English-language translations of foreign scientific and technical material pertinent to NASA's mission.

Specialized services also include creating custom thesauri, building customized databases, organizing and publishing research results.

For more information about the NASA STI program, see the following:

* Access the NASA STI program home page at *http://www.sti.nasa.gov*

* E-mail your question via the Internet to *help@sti.nasa.gov*

* Fax your question to the NASA STI Help Desk at 301–621–0134

* Telephone the NASA STI Help Desk at 301–621–0390

* Write to:
  NASA STI Help Desk
  NASA Center for AeroSpace Information
  7121 Standard Drive
  Hanover, MD 21076–1320

Latest Developments in SLD Scaling

Jen-Ching Tsao and David N. Anderson
Ohio Aerospace Institute, Cleveland, Ohio

National Aeronautics and
Space Administration

Glenn Research Center
Cleveland, Ohio 44135

February 2006

Acknowledgments

This report contains preliminary findings,
subject to revision as analysis proceeds.

Level of Review: This material has been technically reviewed by NASA technical management OR expert reviewer(s).

Available from

Latest Developments in SLD Scaling

Jen-Ching Tsao and David N. Anderson
Ohio Aerospace Institute
Brook Park, Ohio 44142

Scaling methods have been shown previously to work well for super cooled large droplet (SLD) main ice shapes. However, feather sizes for some conditions have not been well represented by scale tests. To determine if there are fundamental differences between the development of feathers for appendix C and SLD conditions, this study used time-sequenced photographs, viewing along the span of the model during icing sprays. An airspeed of 100 kt, cloud water drop MVDs of 30 and 140 μm, and stagnation freezing fractions of 0.30 and 0.50 were tested in the NASA Glenn Icing Research Tunnel using an unswept 91-cm-chord NACA0012 airfoil model mounted at 0° AOA. The photos indicated that the feathers that developed in a distinct region downstream of the leading-edge ice determined the horn location and angle. The angle at which feathers grew from the surface were also measured; results are shown for an airspeed of 150 kt, an MVD of 30 μm, and stagnation freezing fractions of 0.30 to 0.60. Feather angles were found to depend strongly on the stagnation freezing fraction, and were independent of either chordwise position on the model or time into the spray. Feather angles also correlated well with horn angles. For these tests, there did not appear to be fundamental differences between the physics of SLD and appendix C icing; therefore, for these conditions similarity parameters used for appendix C scaling appear to be valid for SLD scaling as well. Further investigation into the cause for the large feather structures observed for some SLD conditions will continue.

Nomenclature

A_c Accumulation parameter (Eq. (6)), dimensionless
b Relative heat factor (Eq. (10)), dimensionless
c Airfoil chord, cm
c_p Specific heat of air, cal/g K
$c_{p,ws}$ Specific heat of water at the surface temperature, cal/g K
d Cylinder radius or twice the leading-edge radius of airfoil, cm
h_c Convective heat-transfer coefficient, $cal/s\,m^2\,K$
h_G Gas-phase mass-transfer coefficient, $g/s\,m^2$
K Inertia parameter (Eq. (2)), dimensionless
K_0 Modified inertia parameter (Eq. (1)), dimensionless
LWC Cloud liquid-water content, g/m^3
MVD Water droplet median volume diameter, μm
n Local freezing fraction, dimensionless
n_0 Stagnation freezing fraction (Eq. (7)), dimensionless
p Pressure, Nt/m^2
p_w Vapor pressure of water in atmosphere, Nt/m^2
p_{ww} Vapor pressure of water at the icing surface, Nt/m^2
r Recovery factor, dimensionless
Re Reynolds number of model (Eq. (11)), dimensionless
$Re\delta$ Reynolds number of water drop (Eq. (3)), dimensionless
s Distance along airfoil surface measured from stagnation line, cm
t_f Freezing temperature, °C
t_s Surface temperature, °C
t Air temperature, °C
T Absolute air temperature, K
V Air velocity, kt
We_L Weber number based on model size and water properties (Eq. (12)), dimensionless
α Angle between feather and chord line, deg

β_0	Collection efficiency at stagnation line (Eq. (5)), dimensionless
ϕ	Droplet energy transfer parameter (Eq. (8)), °C
λ	Droplet range, m
λ_{Stokes}	Droplet range if Stokes Law applies, m
Λ_f	Latent heat of freezing, cal/g
Λ_v	Latent heat of condensation, cal/g
μ	Air viscosity, g/m s
θ	Air energy transfer parameter (Eq. (9)), °C
ρ	Air density, g/m^3
ρ_i	Ice density, g/m^3
ρ_w	Liquid water density, g/m^3
$\sigma_{w/a}$	Surface tension of water over air, dyne/cm
τ	Accretion time, min

Subscripts

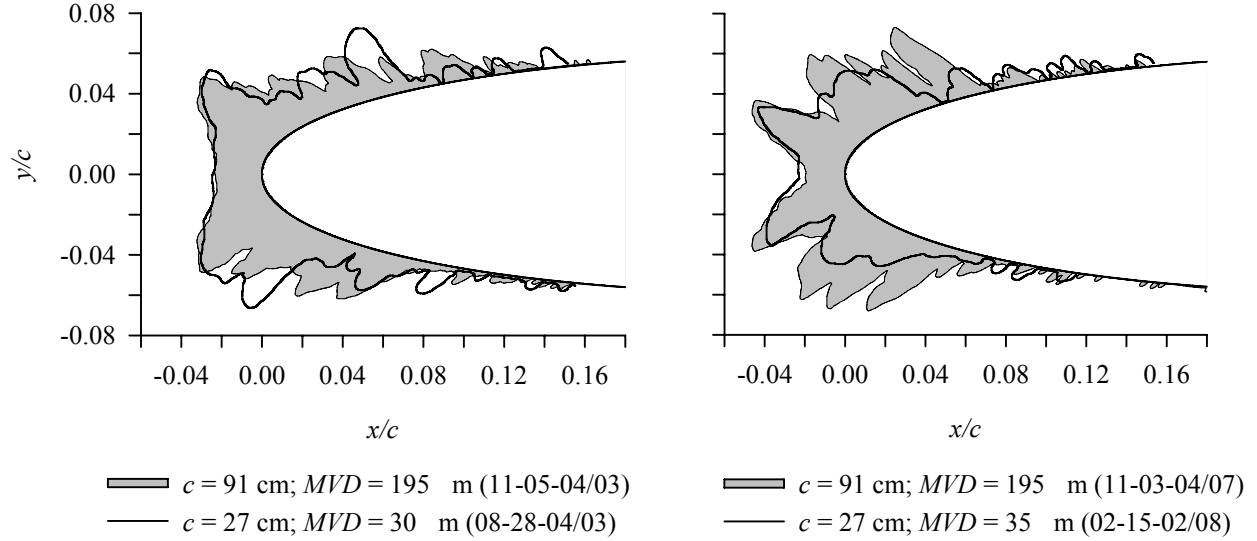| R	reference
S	scale
st	static
tot	total

I. Introduction

Scaling methods for SLD conditions have been under development for several years at NASA Glenn (refs. 1 and 2). These studies established that good simulations of SLD main ice shapes can be achieved at appendix C conditions using existing scaling methods. These methods match scale and reference values of the parameters n_0 and We_L, the product $\beta_0 A_c$ and maintain β_0 within about 10 percent. Figure 1 gives some typical examples of such scaling. Figure 1(a) shows a good simulation of both main ice shape and feather region for a reference velocity of 100 kt with model size scaled from 91 to 27 cm and MVD from 195 to 30 μm. The important similarity parameters were matched within about 10 percent, although the difference in the scale and reference We_L was somewhat larger; apparently, these matches were adequate. In figure 1(b), a reference velocity of 150 kt was used with size scaled again from 91 to 27 cm and MVD from 195 to 30 μm. The main ice shapes matched fairly well, but the scale (appendix C) feathers failed to simulate the large formations recorded in the SLD test. In each of the examples in figure 1 the β_0 for scale and reference differ by only about 4 to 6 percent.

Due to the failure of scaling methods to produce adequate simulations of feather regions in some situations, a study of feather growth has been undertaken (ref. 3). An understanding of the physical phenomena behind feather development and the identification of possible new similarity parameters is important to the improvement of scaling methods for SLD as well as appendix C conditions for at least three reasons. First, the large feather formations observed in some prior SLD studies need to be simulated accurately in scale tests at appendix C conditions. Second, even if feather characteristics for more normal-sized feather growth were not of particular interest in scaling, ice shape tracings indicate that feather and horn angle may be related. Thus, the same phenomena that determine feather angle may also regulate horn angle. Third, the same phenomena and similarity parameters governing straight-wing feather growth probably also control swept-wing ice scallop formation.

A first step in identifying any new similarity parameters for inclusion in scaling methods is to understand what differences there might be between SLD and appendix C feathers. In reference 3 the feather region was studied through close-up photographs to identify characteristics of feather appearance that might help to determine if there are differences between appendix C and SLD regimes. The authors were unable to determine any differences in the structural appearance of feathers formed at the same freezing fraction under the two regimes. Some differences in SLD and appendix C feather angles were reported at a speed of 200 kt, but additional data are needed to confirm these results and to cover a wider range of conditions.

This paper presents the latest results in the examination of feather formation. Icing tests were performed at a velocity of 100 kt during which a sequence of still pictures were taken from an overhead camera every 10 sec to record both leading-edge and feather ice development. Drop MVDs were 30 and 140 μm and the stagnation freezing fractions were 0.30 and 0.50 for these studies. Feather-angle measurements will also be shown for a velocity of 150 kt, an MVD of 30 μm and stagnation freezing fractions from 0.30 to 0.60. All tests were performed in the NASA Glenn IRT using a full-span, 91-cm-chord NACA 0012 straight-wing airfoil model mounted at 0° AOA.

	c = 91 cm; MVD = 195 m (11-05-04/03)
	c = 27 cm; MVD = 30 m (08-28-04/03)

(a) V_R, 100 kt.

	c = 91 cm; MVD = 195 m (11-03-04/07)
	c = 27 cm; MVD = 35 m (02-15-02/08)

(b) V_R, 150 kt.

Date/Run	c, cm	t_{st}, °C	V, kt	MVD, µm	LWC, g/m³	τ, min	β_0, %	A_c	$\beta_0 A_c$	n_0	Re, 10^4	We_L, 10^6
(a) 11-05-04/03	91.4	-18	100	195	1.46	11.0	96.2	1.87	1.80	0.49	12.1	1.18
08-24-04/03	26.7	-9	200	30	0.50	4.6	90.1	1.84	1.66	0.53	6.4	1.37
(b) 11-03-04/07	91.4	-17	149	195	1.00	10.7	96.8	1.86	1.80	0.50	17.7	2.61
02-15-02/08	26.7	-15	276	35	0.64	2.7	93.0	1.89	1.76	0.50	8.5	2.61

Figure 1.—Examples of scaling from SLD to appendix C conditions (ref. 3). NACA 0012 models; chord scaled from 91 to 27 cm; n_0, 0.5.

II. Similarity Parameters

The similarity parameters used in this study were based on the work originally done by Ruff (ref. 4). Descriptions and derivations are also given in Anderson (refs. 5 and 6).

The modified inertia parameter, K_0, was defined by Langmuir and Blodgett (ref. 7):

$$K_0 = \frac{1}{8} + \frac{\lambda}{\lambda_{Stokes}}\left(K - \frac{1}{8}\right) \tag{1}$$

In equation (1), K is the inertia parameter,

$$K = \frac{\rho_w MVD^2 V}{18 d \mu} \tag{2}$$

where d is the cylinder radius or twice the leading-edge radius of curvature for airfoils. For the NACA 0012 airfoil model, a leading-edge radius of $0.0158c$ was used (see Abbott and von Doenhoff (ref. 8)), where c is the model chord. λ/λ_{Stokes} is the droplet range parameter, defined as the ratio of actual droplet range to that if Stokes drag law for solid-spheres applied. It is a function only of the droplet Reynolds number, Re_δ.

$$Re_\delta = \frac{V MVD \rho}{\mu} \tag{3}$$

Langmuir and Blodgett's tabulation of the range parameter was fit to the following expression for this study:

$$\frac{\lambda}{\lambda_{Stokes}} = \frac{1}{\left(0.8388 + 0.001483 Re_\delta + 0.1847\sqrt{Re_\delta}\right)} \tag{4}$$

Of more practical interest than K_0 is the collection efficiency at the stagnation point, β_0, which was shown by Langmuir and Blodgett to be a function only of K_0,

$$\beta_0 = \frac{1.40\left(K_0 - \frac{1}{8}\right)^{.84}}{1 + 1.40\left(K_0 - \frac{1}{8}\right)^{.84}} \tag{5}$$

The accumulation parameter is:

$$A_c = \frac{LWC\,V\,\tau}{d\,\rho_i} \tag{6}$$

If all the water impinging on the leading edge freezes at that location and the leading-edge collection efficiency is 100 percent, A_c is a measure of the normalized thickness of ice that will accrete.

The freezing fraction is defined as the ratio of the mass of water that freezes at a given location on the surface to the total mass of water that impinges the surface at that location. From Messinger's (ref. 9) steady-state surface energy balance formulation, the stagnation freezing fraction is

$$n_0 = \frac{c_{p,ws}}{\Lambda_f}\left(\phi + \frac{\theta}{b}\right) \tag{7}$$

The individual terms in this expression are ϕ, the water energy transfer parameter, θ, the air energy transfer parameter, and b, the relative heat factor, introduced by Tribus, et al. (ref. 10)

$$\varphi = t_f - t_{st} - \frac{V^2}{2c_{p,ws}} \tag{8}$$

$$\theta = \left(t_s - t_{st} - r\frac{V^2}{2c_p}\right) + \frac{h_G}{h_c}\left(\frac{\dfrac{p_{ww}}{T_{st}} - \dfrac{p_{tot}}{T_{tot}}\dfrac{p_w}{p_{st}}}{\dfrac{1}{.622}\dfrac{p_{tot}}{T_{tot}} - \dfrac{p_{ww}}{T_{st}}}\right)\Lambda_v \tag{9}$$

$$b = \frac{LWC\,V\,\beta_0\,c_{p,ws}}{h_c} \tag{10}$$

Equation (9) given by Ruff includes compressibility effects. Simpler forms without compressibility have also been used by Charpin and Fasso (ref. 11) and others, but the differences in values are not significant.

The Reynolds and Weber numbers of the model, Re, are based on the twice the nose radius of the airfoil:

$$Re = \frac{V d \rho}{\mu} \tag{11}$$

$$We_L = \frac{V^2 d \rho_w}{\sigma_{w/a}} \tag{12}$$

III. Test Description

A. Facility, Model and Procedures

The icing tests were performed in the NASA Glenn Icing Research Tunnel (IRT). The IRT is a closed-loop, refrigerated, sea-level tunnel with a 1.8 by 2.7 m rectangular test section. The icing cloud is generated by operating 10 spray bars, a configuration in use since 1998.

The IRT cloud calibrations for both appendix C and SLD conditions used for these tests was performed in the summer of 2004. The *LWC* and *MVD* measurements were made using methods reported previously (ref. 12). However, drop-sizing instruments have been updated from past calibration work. Thus, the definition of *MVD* for a particular cloud may differ from interpretations previously reported, particularly for the SLD regime. For example, for given spray-bar pressures, the latest calibration gives *MVD*s of 85 to 95 percent of those obtained in a 2002 calibration. The *MVD*s reported in this paper are based on an analysis of the *MVD* calibration data completed in November, 2004.

The model was a 91.4-cm-chord fiberglass NACA 0012 airfoil mounted vertically on the tunnel turntable at 0° angle of attack and 0° sweep. It is shown in figure 2 installed in the IRT test section. It extended from floor to ceiling (183-cm span). Horizontal lines at the leading edge were drawn at the tunnel vertical center (model mid span) and ±2.5 cm from the center to locate ice-tracing templates. Vertical lines were also placed at increments of 2.5 cm (labeled in inches on the model), measured along the surface from the stagnation line. These marks helped to identify sites on the model for close-up photographs of feather structure details. Because of the quick-start capability of the IRT spray system, no shielding of the models was required during the initiation of the spray.

A digital camera was mounted on the third floor of the IRT to view the model from above (i.e., along the span) through transparent windows on the ceiling of the test section. Portions of both the horn and feather region of the lower surface were in the camera view. The shutter and an independent flash were remotely operated with an automatic signal to take a sequence of still images every 10 sec throughout the spray. Spray durations were 14 to 28 min for these tests. The stills were later assembled into movies of the ice-accretion development.

In preparing for a test, the temperature and airspeed in the test section and the air and water pressures on the spray manifolds were set. When these conditions had stabilized, the spray nozzle valves were opened to initiate the spray. The spray was timed for the required duration, then turned off. The fan was brought to a full stop and the researchers entered the test section to document the ice shape with hand tracings. Close-up photographs were also taken with a hand-held digital camera.

To record the ice shapes, a thin slice was first melted through the ice normal to the model surface. A cardboard template was then placed into this slit and an outline of the ice shape traced by pencil, giving a two-dimensional cross section of the ice. Tracings were taken at the vertical center of the tunnel (91 cm from the floor) and at 2.5 cm above the center. The ice shapes so recorded were digitized using an automated line-following feature in SigmaScan Pro (ref. 13) software. Only tracings taken at the model midspan (tunnel vertical center) will be presented.

After the ice tracings were obtained, the tracing template was removed and a thin plate on which was printed an orthogonal grid was placed in the mid-span slit. Photographs of feathers in several chord-wise locations on both sides of the model were taken with the hand-held camera looking spanwise along the airfoil surface with the grid in the background. The camera lens was placed as close to the model as possible to avoid distortion of the grid, although some distortion was inevitable. For each test three to five pictures were taken altogether, including photos of both the lower surface and upper surface feather regions. From these images, the feather angle was determined.

The results presented are from IRT test entries in February 2005.

B. Uncertainty Analysis

Estimates of the uncertainty in the reported average conditions were made by considering inherent errors of instruments, temporal fluctuation and spatial variation of the instrument readings in the test section, and uncertainty in tunnel calibration of *MVD* and *LWC*. Recorded air temperature was believed to be accurate to ±0.5°C, and the uncertainty in air velocity was estimated to be ±1m/s. For

Figure 2.—91.4-cm-chord, 183-cm-span fiberglass NACA 0012 airfoil models installed in IRT test section.

appendix C conditions the net uncertainty in MVD was estimated at ±12 percent. For SLD conditions it may have been as much as ±20 percent. These uncertainties are not referenced to an absolute value of MVD, which is unknown. Repeatability and scatter in the LWC calibration data suggests the uncertainty is about ±12 percent for both appendix C and SLD conditions.

The test-parameter uncertainties were used to estimate the following uncertainties in the similarity parameters for the appendix C tests: 9 percent in β_0, 12 percent in A_c, 13 percent in n_0, 3 percent in Re, and 5 percent in We_L. For the SLD tests the uncertainties were: 3 percent in β_0, 12 percent in A_c, 11 percent in n_0, 3 percent in Re, and 5 percent in We_L.

Feather-angle uncertainties were due primarily to subjective determination of the direction of growth of a feather. For very small feathers (e.g., early in a test or near the icing limit) the uncertainty may be as much as 10°, and for large feathers, only 5°. At the lowest stagnation freezing fraction tested ($n_0 = 0.30$) glaze feathers were often not as well defined as those for higher freezing fractions, leading to further uncertainty of perhaps 5° to 10°. Independent analysis of a limited number of images by two researchers led to differences in average feather angle of 2° to 4°. It is estimated that additional errors of 5° to 10° could result from distortions of the grid used to calibrate the distances in an image.

IV.   Results

A. Feather and Ice-Shape Development

Photographs were taken every 10 sec with the overhead camera looking down along the span of the model. The view of this camera is shown in figure 3. The interpretations of ice development presented here are based on these photographs. Only glaze accretions will be discussed.

Feathers typically developed from a narrow base at the surface of the model, growing wider in the spanwise direction with time. Thus, the resulting structure typically had a trapezoidal profile when viewed in the airflow direction, but had a relatively uniform thickness in the chordwise direction. The height of the individual feathers and the number of feathers diminished with distance from the leading edge, following the collection-efficiency decrease. Most feathers, particularly farther aft on the model, were very fragile, and sometimes little more than a touch was sufficient to break them loose. Feather shedding from time to time occurred during the ice accretion process, but only a relatively small number were lost from the final accretion for the conditions of these tests. Nearer the leading edge, feathers were at such a density that they grew together to form large structures. The main-shape horns were typically incorporated into these growths and indistinguishable from them.

The non-reflective surface of the fiberglass model is apparent from the image of figure 3. This photo was taken at the beginning of a test just before the spray actually wetted the model. A sampling of the sequence of photos that followed that of figure 3 is shown in figure 4. The conditions for the test of figure 4 included a velocity of 100 kt, an MVD of 140 μm and a stagnation freezing fraction of 0.30. Complete details of test conditions for figures 4 to 9 are give in table I.

The first frame in figure 4 was taken just 3 sec after that of figure 3. By this time, the model was wet from the spray, as evidenced by the red reflection from the tunnel floor that appeared in the leading-edge surface. Approximately 30 sec later (2nd frame), discrete feathers were visible about 2.5 to 5 in. aft of the stagnation. Thus, almost immediately, two separate areas of accretion became apparent: a leading-edge region in which the surface was covered with a film of water or ice, and a feather region characterized by discrete spikes of ice seeming to grow directly from the clean airfoil surface.

02-11-05/02 2088

Figure 3.—Clean model before onset of spray.
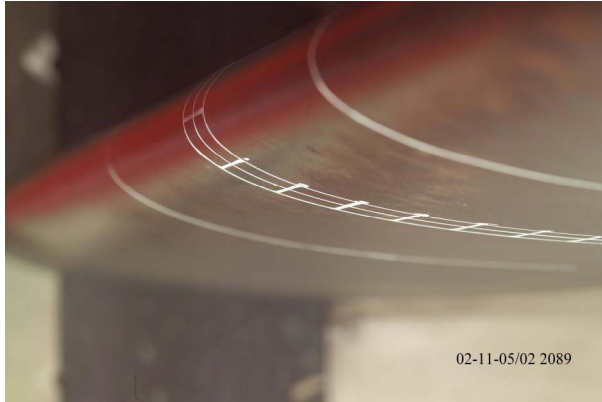
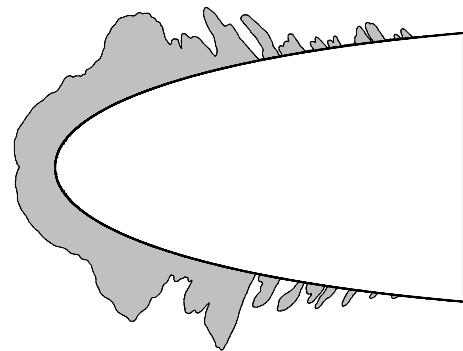Spray hits model.
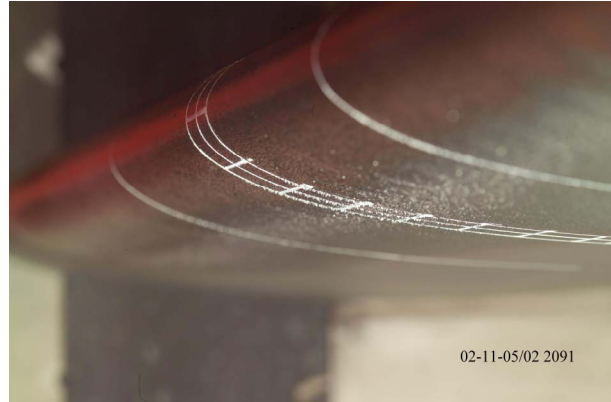
30 sec

105 sec

460 sec

920 sec

Centerline ice profile at end of spray.

Figure 4.—Ice accretion development for 140-µm *MVD* and n_0 = 0.30. 02-11-05 Run 2. *c*, 91.4 cm; *V*, 100 kt; β_0, 94 percent; $\beta_0 A_c$, 1.80.

Several studies (refs. 14, 15, and 16) using high-magnification photography over the last 20 years have led to a detailed description of the leading-edge region that was not examined in the present work. From these previous investigations, we know that for short accretion times, the leading-edge region can be subdivided into smooth and rough zones. The smooth zone extends aft from the stagnation line on both the lower and upper surfaces of the model, followed by transition to a rough zone. The rough zone is characterized by a distribution of small, hemispherical roughness elements over the surface (ref. 16). As accretion progresses the smooth-rough boundary moves

TABLE I.—TEST CONDITIONS FOR FIGURES 4 TO 9

Figure	Date/Run	c, cm	t_{st}, °C	V, kt	MVD, μm	LWC, g/m³	τ, min	β_0, %	A_c	$\beta_0 A_c$	n_0
4, 5	02-11-05/02	91.4	-9	100	140	1.17	14.0	94.4	1.91	1.80	0.30
6, 7	02-11-05/05	91.4	-15	100	140	1.17	14.0	94.4	1.91	1.80	0.50
8, 9	02-11-05/03	91.4	-9	100	30	0.80	28.0	68.9	2.61	1.80	0.50

upstream toward the stagnation. In figure 4, this narrowing of the smooth zone with time can be inferred from the shrinking of the width of the red reflection at the leading edge.

An abrupt transition took place from the leading-edge region to the feather region. The location of this transition was determined when the local freezing fraction, increasing with distance from the stagnation, reached a value sufficiently high to permit rapid freezing. Because β decreases with distance, those feathers at the transition grew the fastest and became the largest in the feather region. Feathers were also more dense in this location and tended to merge together as they developed, forming a barrier. Unfrozen surface water moving aft in the leading-edge region was prevented from further motion both by the physical obstruction of the feather structures at the transition site as well as by the high rate of freezing there. Liquid water reaching this location would tend to flow into these merged feathers, to fill voids in the feathers, and then to freeze to contribute to the structure. In this way, the ice horns formed.

Figure 5 illustrates some of these features for the test of figure 4. It is a photograph of a portion of the feather region on the upper surface of the model taken at the completion of the test using the hand-held digital camera. The leading edge of the model is to the right in this picture, and during the spray, flow was from right to left. The discrete nature of the feathers is apparent, as is the fact that between the feathers there is no frozen water on the surface. On the right of the photograph, the largest feathers can be seen. Beyond them and out of focus in the background is the aft plane of the upper-surface horn. On close inspection feather structures can be seen embedded into the downstream surface of the horn.

Other than the interaction at the transition, the two regions appeared to continue to develop independently. At 105 sec in figure 4 the feathers were just discernible, while the rough zone of the leading-edge region has spread forward nearly to the stagnation line. At 460 sec the largest feathers had reached a significant size, and in the leading-edge region the rough zone now extended all the way to the stagnation line. The frame at 920 sec was taken just after the spray ended. The largest feathers continued to grow up to this point, but smaller feathers further aft ceased to develop after about 460 sec, presumably because they were shielded from the spray once the larger feathers reached a certain size. The spanwise variation in the width of the leading-edge ice from horn to horn is due to IRT cloud non-uniformities in LWC.

The two-dimensional profile of the final ice shape appears in the lower right panel of figure 4. The difference between the continuous-ice accretion within the leading-edge region and the discrete isolated structures of the feather region is again apparent. At the transition between the two regions, water has frozen over the upstream surfaces of the largest feathers to form a continuous spanwise horn structure on both the pressure and suction sides of the model.

Figure 5.—Feather region and aft plane of horn on upper surface at the completion of the spray of figure 4. 02-11-05 run 2. c, 91.4 cm; V, 100 kt; MVD, 140 μm; β_0, 94 percent; $\beta_0 A_c$, 1.80; n_0, 0.30.

Figure 6 presents a series of photographs taken during an accretion with only temperature changed from the test shown in figure 4. This change resulted in an increase in the stagnation freezing fraction from 0.30 to 0.50. Although the collection efficiency was the same as for figure 4, the higher n_0 for the case of figure 6 caused the location of the transition from the leading-edge to the feather region to move forward. Because transition occurs when the local freezing fraction is sufficiently high, this result is not surprising. Other than the narrower leading-edge region and wider feather region, the development of ice in the two regions appeared to progress much the same as it did in the
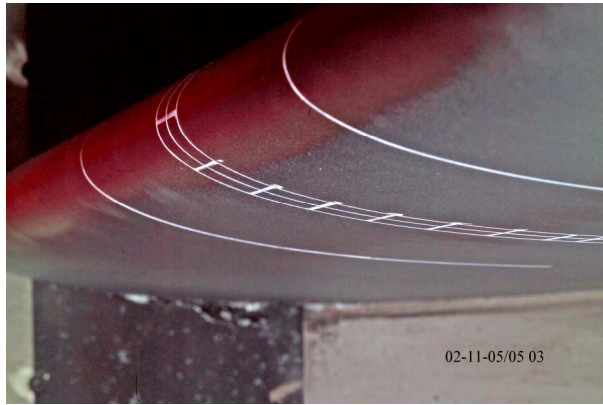
Spray hits model.

30 sec

90 sec

170 sec

840 sec
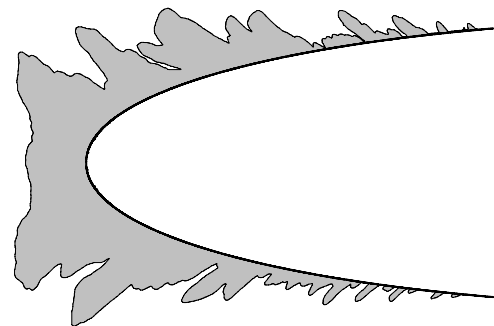
Centerline ice profile at end of spray.

Figure 6.—Ice accretion development for 140-μm *MVD* and n_0 = 0.50. 02-11-05 Run 5. *c*, 91.4 cm; *V*, 100 kt; β_0, 94 percent; $\beta_0 A_c$, 1.80.

case of figure 4. Once again, the horn grew at the site of transition from continuous leading-edge ice to discrete feather growth. The last frame of the figure, at the lower right, shows the ice profile traced at the completion of the spray.

Figure 7 is a close-up photograph of the feathers on the lower surface, taken with the hand-held camera after the spray had ended. During the spray, the flow was from left to right. Compared to the feathers in figure 5, those in figure 7 were characterized by fine branches that grew from the core. At the lower n_0 of figure 5 water would have taken longer to freeze on the feather, tending to fill in any branches. Measurement of feather angle also revealed that the higher stagnation freezing fraction of figure 7 produced a smaller feather angle with respect to the chord line of the model compared with that of figure 5. Thus, feather appearance and angle were both dependent on the freezing fraction.

A third photographic sequence showing ice development is given in figure 8. The velocity and stagnation freezing fraction for this icing encounter are the same as for that of figure 6. However, the *MVD* has been reduced from 140 to 30 μm to investigate possible differences between SLD and appendix C accretions. No change in the way appendix C and SLD feathers cover the surface initially and subsequently develop can be seen from the photos, except that the lower collection efficiency for the appendix C case resulted in a feather region that did not extend as far aft as that of the SLD situation in figure 6. Due to the lower collection efficiency feathers did not grow as quickly for the appendix C encounter.

The ice shape traced at the completion of the 30-μm test is shown in the last frame of figure 8. The profile is of a similar shape compared with the 140-μm test of figure 6, but both the horns and feathers were smaller. In order to compare tests with the same velocity but different drop size, it was not possible to scale the conditions of figures 6 and 8. In particular, β_0 could not be matched for the two tests. The differences in the profiles can be attributed to the reduced β_0 for the encounter of figure 8 compared with the conditions of figure 6. For scaling, clearly it is important to try to match the scale-test β_0 as closely to that determined by the reference conditions as possible.

Figure 9 shows a portion of the lower surface feather region and the aft side of the lower horn as photographed in the test section with the hand-held camera after the test of figure 8. The flow is from left to right in this picture. At the left is the aft plane of the lower surface horn and some of the feathers can be seen imbedded into this surface. The discrete nature of the feathers farther aft is apparent. The delicate branches and narrow base of these feathers, formed with a 30-μm spray, were also seen with the 140-μm-spray feathers documented in figure 7. Fundamental differences between appendix C and SLD feathers were not evident.

Figure 7.—Feather region and aft plane of horn on lower surface at the completion of the spray of figure 6. 02-11-05 Run 5. *c*, 91.4 cm; *V*, 100 kt; *MVD*, 140 μm; β_0, 94 percent; $\beta_0 A_c$, 1.80; n_0, 0.50.
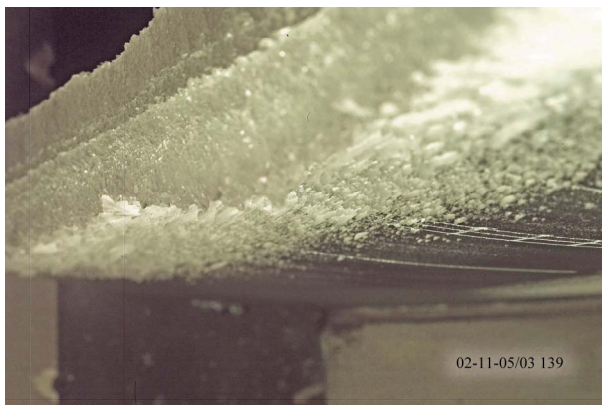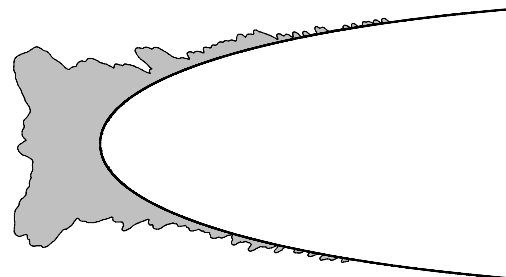
Spray hits model.

73 sec

241 sec

881 sec

1381 sec

Centerline ice profile at end of spray.

Figure 8.—Ice accretion development for 30-μm *MVD* and n_0 = 0.50. 02-11-05 Run 3. *c*, 91.4 cm; *V*, 100 kt; β_0, 69 percent; $\beta_0 A_c$, 1.80.

02-11-05/03 40594

Figure 9.—Lower surface horn aft plane and feather region at the completion of the spray of figure 8. 02-11-05 Run 3. c, 91.4 cm; V, 100 kt; MVD, 30 μm; β_0, 69 percent; $\beta_0 A_c$, 1.80; n_0, 0.50.

B. Feather Angle

The angle at which the feathers grow relative to the chord line was introduced into the study of reference 3 as a quantitative characteristic to complement close-up photos of feather appearance. It was reasoned that if appendix C and SLD feathers showed markedly different angles, it might be logical to conclude that the processes controlling feather growth were also different. While some differences were seen between the two regimes, they were small enough to conclude, at least tentatively, that the physics of formation were probably fundamentally the same. Data were limited, however.

Feather angles were measured again for the tests of this study to supplement the data of reference 3. The feather angle reported is that defined in figure 10 for both a lower-surface (fig. 10(a)) and an upper-surface feather (fig. 10(b)). In either case, angles were recorded as positive, and no distinction was made in reporting results to indicate which surface was analyzed.

The angle was determined by photographing the feather region of the accretion against a background of a dimensioned orthogonal grid. Figure 11 is an example of such a photo taken in the test section with the hand-held camera at the completion of one of the sprays. Some of the photographs taken during the spray from the overhead camera were also used for angle measurements by digitally superimposing an orthogonal grid on the image. For images from both sources, the grid provided calibration information for both x and y dimensions. The angle was then found from the image using the angle-measuring capability of SigmaScan Pro software (ref. 13). The chordwise location of the feather root and its angle were both recorded for well-defined feathers in each photograph. The angle was found to be independent of distance from stagnation; therefore, only ensemble average angles will be reported. Angles measured from different photos from the same test showed no significant differences within the scatter of data, and data from all the photographs for a particular test were included in determining average values for that test.

For each test condition, feather-angle data were obtained from the overhead pictures taken during the test for times of approximately 12 and 100 percent of the total spray time. In figure 12 sample results from these within-spray photos are compared with angles measured from the after-test pictures taken within the test section. These tests used an MVD of 30 μm at a velocity of 150 kt. Within the uncertainty of the data the feather angle did not change with time as the ice accreted and feathers grew. Furthermore, angles measured from the two photo sources were consistent. Although the local collection efficiency at a feather site must increase as the feather grows, the results of figure 12 suggest that the mechanism of feather formation that determines angle does not change significantly, it at all, from the time feather
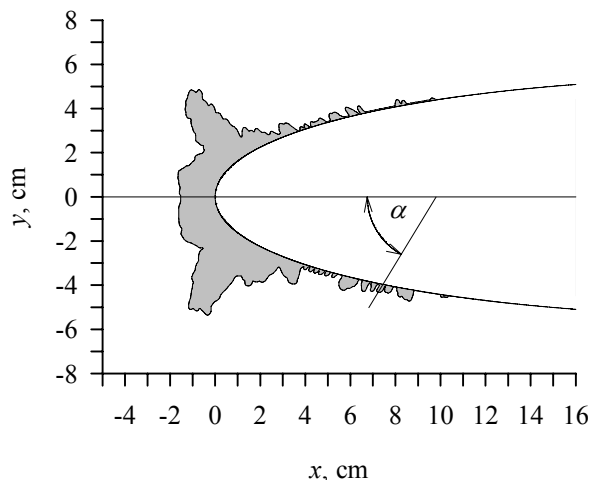
(a) Feather angle measured on lower surface.
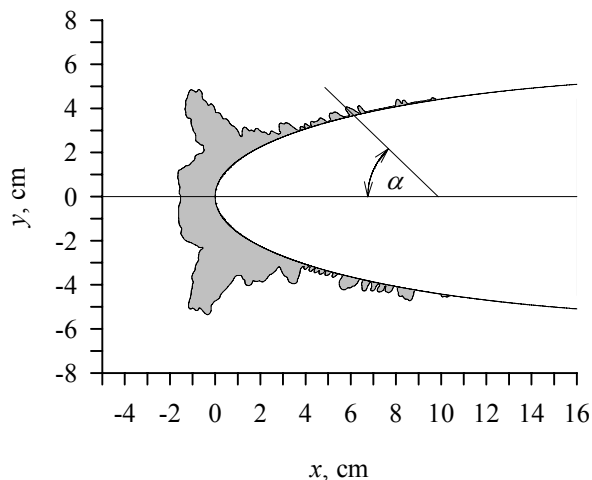
(b) Feather angle measured on upper surface.

Figure 10.—Definition of feather angle. c, 36 in; V, 150 kt; MVD, 30 μm; n_0, 0.30.
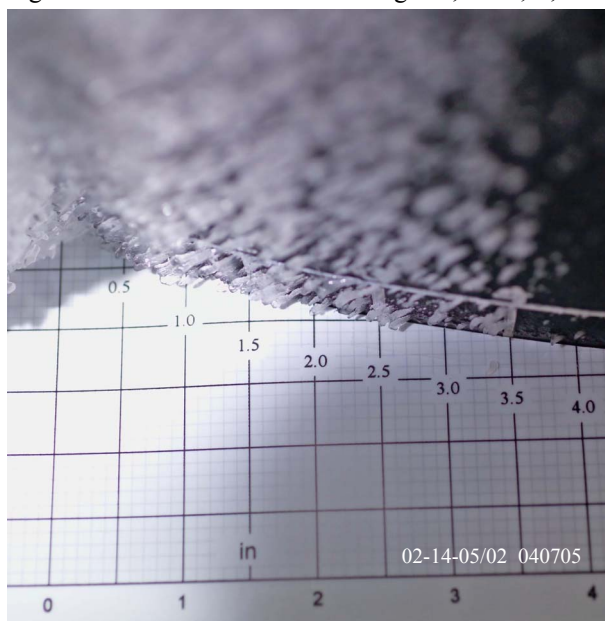

Figure 11.—Feathers photographed against a grid for angle measurement. Horizontal grid lines are parallel to chord line. Major grid lines every 0.5 in. c, 91.4 cm; V, 150 kt; MVD, 30 μm; n_0, 0.40.
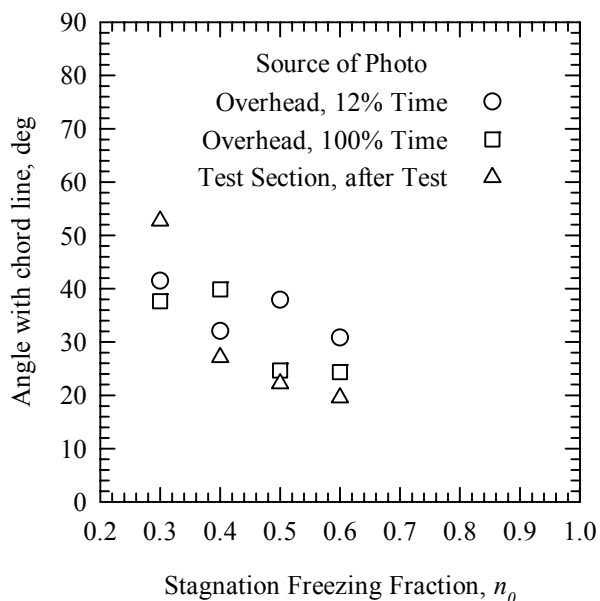

Figure 12.—Feather angle at multiple times into spray. c, 91.4 cm; V, 150 kt; MVD, 30 μm.

growth begins until the spray is completed. The trend observed in reference 3, in which feather angle decreased with increasing stagnation freezing fraction, is also apparent in this figure.

The horn angle was determined by averaging the horn upstream-surface angle and the horn aft-surface angle with respect to the chord line. These angles were measured from the ice-profile tracings. Figure 13 illustrates the resulting horn angle. Horn angles are compared in figure 14 with those feather angles that were recorded after the test. For this comparison, only the lower horn angle was used. The horn angle was always greater than the feather angle and showed the same decreasing trend with increasing stagnation freezing fraction. This result is consistent with the mechanism of horn formation postulated above, in which the location and angle of those feathers nearest the leading edge of the airfoil determine both horn location and angle.
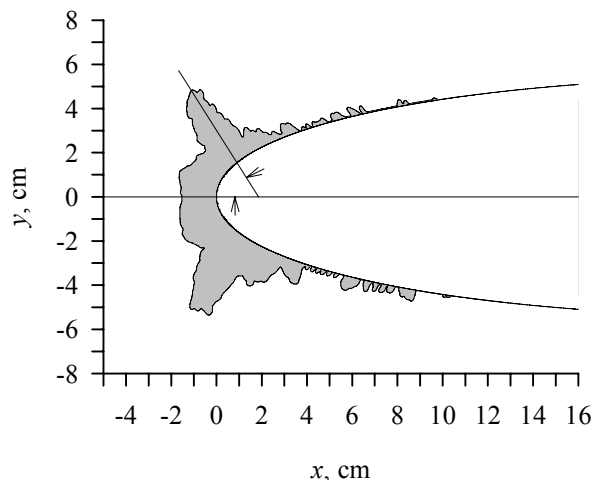
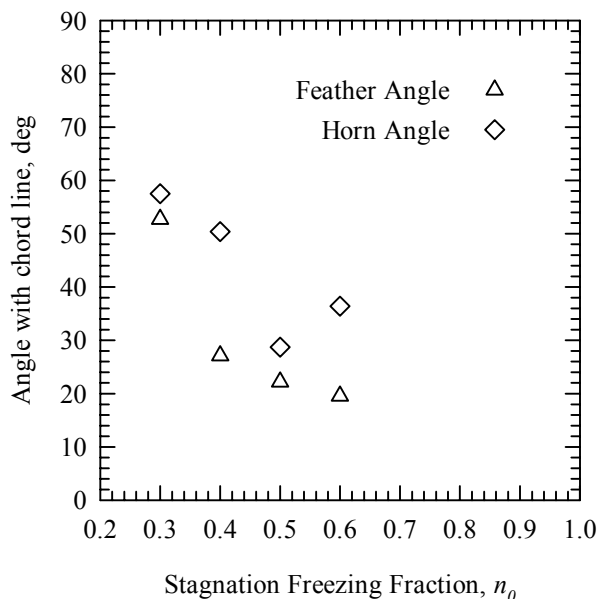Figure 13.—Definition of horn angle. *c*, 36 in; *V*, 150 kt; *MVD*, 30 μm; n_0, 0.30.

Figure 14.—Comparison of horn angles with final feather angles. *c*, 91.4 cm; *V*, 150 kt; *MVD*, 30 μm.

V. Summary and Concluding Remarks

Icing tests were performed using a 91-cm-chord NACA 0012 airfoil for both SLD and appendix C conditions with the objective of identifying differences in feather formation for the two icing regimes. All tests were for glaze conditions, with stagnation freezing fractions of 0.30 to 0.50. Images taken 10 sec apart during the spray showed two major, distinct regions of ice growth from the time the spray first impacted the model: the leading-edge region, in which a thin film forms over the surface, and the feather region, in which small discrete feathers appeared, apparently from direct-impingement of drops in the spray cloud.

The feather region began some distance aft of the stagnation and extended to the impingement limit. The angle at which feathers grew relative to the chord line was found to be independent of time and position, but was a strong function of stagnation freezing fraction. Because the local collection efficiency decreases with distance from the stagnation line, feathers at the front of the feather region grew fastest and became the largest. Fairly soon into the spray, these upstream feathers grew together. The resulting structure would tend to form a barrier, preventing leading-edge-region surface water from flowing further aft. So blocked, this water would flow into and freeze onto the upstream face of the feather structure, producing glaze horns. This conclusion that feathers determine the location and angle of the horns in glaze icing encounters was substantiated by the fact that the horn angle was found to correlate with the feather angle. At some point, the larger upstream feathers captured cloud water droplets efficiently enough to shield the smaller downstream feathers from the cloud, and the latter ceased to grow. Analysis of photos and ice tracings taken at the completion of the spray showed that feather growth angle decreased with increasing stagnation freezing fraction.

For the limited conditions of this study, there was no evidence of any difference in the fundamental formation mechanisms of either feather growth or horn formation between SLD and appendix C conditions. This conclusion is consistent with the findings of reference. However, SLD reference and appendix C scale tests performed in the past have shown that while the main ice shape could be matched nondimensionally, relatively larger feathers occurred for the SLD tests. Therefore, reasons for large feather formations other than unique physics of SLD icing need to be investigated. Potential causes of the feather-size differences for scaling tests include a mismatch of β_0 for some scaling tests, differences in shedding of feathers at the disparate model sizes and velocities required for scaling, and dissimilarities in the cloud *MVD* distributions for SLD and appendix C conditions. Each of these causes has a different implication for scaling. If a better match of β_0 provides the feather agreement needed, the similarity parameters used in appendix C scaling methods can be used for SLD scaling as well. If feather shedding at the higher scale speeds explains the smaller relative feather sizes for scale models, new similarity parameters will be needed to include shedding analysis in the scaling methodology. If the IRT nozzles generate cloud drop-size distributions that are

different for SLD and appendix C *MVD*s, ways to alter these distributions will need to be considered. Future research is being directed toward looking at each of these issues in order to resolve the feather-size issue and develop better SLD scaling methods.

References

1. Anderson, David N., "A Preliminary Study of Ice-Accretion Scaling for SLD Conditions," AIAA–2002–0521, January 2002.
2. Anderson, David N. and Tsao, J.C., "Additional Results of Ice-Accretion Scaling at SLD Conditions," AIAA–2003–0390, January 2003.
3. Tsao, Jen-Ching and Anderson, David N., "Further Assessment of MVD Effects in SLD Applications," AIAA–2005–0072, January 2005.
4. Ruff, G.A., "Analysis and Verification of the Icing Scaling Equations," AEDC-TR-85-30, vol. 1 (rev), March 1986.
5. Anderson, David N., "Manual of Scaling Methods," NASA/CR—2004-212875, March 2004.
6. Anderson, David N. and Tsao, J.C., "Overview of Icing Physics Relevant to Scaling," FAA In-Flight Icing/Ground De-icing International Conference & Exhibition, SAE-2003-01-2130, June 16–20, 2003.
7. Langmuir, Irving and Blodgett, Katharine B. "A Mathematical Investigation of Water Droplet Trajectories," Army Air Forces Technical Report No. 5418, February 1946.
8. Abbott, Ira H. and von Doenhoff, Albert E., *Theory of Wing Sections*, Dover, New York, 1959, pp. 114 and 321.
9. Messinger, B.L., "Equilibrium Temperature of an Unheated Icing Surface as a Function of Airspeed," *J. Aeron. Sci.*, vol. 20 no. 1, January 1953, pp. 29–42.
10. Tribus, Myron, Young, G.B.W. and Boelter, L.M.K., "Analysis of Heat Transfer Over a Small Cylinder in Icing Conditions on Mount Washington," *Trans. ASME*, vol. 70, November 1948, pp. 971–976.
11. Charpin, Francois and Fasso, Guy, "Essais de givrage dans la grande soufflerie de Modane sur maquettes a echelle grandeur et echelle reduite," *L'Aeronautique et l'Astronautique*, no. 38, 1972, pp. 23–31. English translation published as "Icing Testing in the Large Modane Wind-Tunnel on Full-Scale and Reduced Scale Models," NASA TM–75373, March 1979.
12. Ide, Robert F. and Oldenburg, John R., "Icing Cloud Calibration of the NASA Glenn Icing Research Tunnel," AIAA–2001–0234, January 2001.
13. SigmaScan Pro, image-processing software, version 5.0, Systat Software, Inc., Point Richmond, CA.
14. Olsen, W. and Walker, E., "Experimental Evidence for Modifying the Current Physical Model for Ice Accretion on Aircraft Structures," NASA TM–87184, May 1986.
15. Hansman, R. John, Jr., Reehorst, Andrew and Sims, James, "Analysis of Surface Roughness Generation in Aircraft Ice Accretion," AIAA–92–0298, January 1992.
16. Shin, Jaiwon, "Characterization of Surface Roughness Associated with Leading Edge Ice Accretion," NASA TM–106459, January 1994 and *J. Aircraft*, vol. 33, no. 2, pp. 316–321, March–April 1996.

1. AGENCY USE ONLY (Leave blank)	2. REPORT DATE	3. REPORT TYPE AND DATES COVERED
	February 2006	Final Contractor Report

4. TITLE AND SUBTITLE

Latest Developments in SLD Scaling

5. FUNDING NUMBERS

WBS–22–077–41–17
NCC3–884
NCC3–938

6. AUTHOR(S)

Jen-Ching Tsao and David N. Anderson

7. PERFORMING ORGANIZATION NAME(S) AND ADDRESS(ES)

Ohio Aerospace Institute
22800 Cedar Point Road
Brook Park, Ohio 44142

8. PERFORMING ORGANIZATION REPORT NUMBER

E–15461

9. SPONSORING/MONITORING AGENCY NAME(S) AND ADDRESS(ES)

National Aeronautics and Space Administration
Washington, DC 20546–0001

10. SPONSORING/MONITORING AGENCY REPORT NUMBER

NASA CR—2006-214127
AIAA–2005–5187

12a. DISTRIBUTION/AVAILABILITY STATEMENT

Unclassified - Unlimited
Subject Category: 03

Available electronically at http://gltrs.grc.nasa.gov

This publication is available from the NASA Center for AeroSpace Information, 301–621–0390.

12b. DISTRIBUTION CODE

13. ABSTRACT (Maximum 200 words)

Scaling methods have been shown previously to work well for super cooled large droplet (SLD) main ice shapes. However, feather sizes for some conditions have not been well represented by scale tests. To determine if there are fundamental differences between the development of feathers for appendix C and SLD conditions, this study used time-sequenced photographs, viewing along the span of the model during icing sprays. An airspeed of 100 kt, cloud water drop *MVD*s of 30 and 140 μm, and stagnation freezing fractions of 0.30 and 0.50 were tested in the NASA Glenn Icing Research Tunnel using an unswept 91-cm-chord NACA0012 airfoil model mounted at 0° AOA. The photos indicated that the feathers that developed in a distinct region downstream of the leading-edge ice determined the horn location and angle. The angle at which feathers grew from the surface were also measured; results are shown for an airspeed of 150 kt, an *MVD* of 30 μm, and stagnation freezing fractions of 0.30 to 0.60. Feather angles were found to depend strongly on the stagnation freezing fraction, and were independent of either chordwise position on the model or time into the spray. Feather angles also correlated well with horn angles. For these tests, there did not appear to be fundamental differences between the physics of SLD and appendix C icing; therefore, for these conditions similarity parameters used for appendix C scaling appear to be valid for SLD scaling as well. Further investigation into the cause for the large feather structures observed for some SLD conditions will continue.

14. SUBJECT TERMS

Icing physics; Scaling; SLD; LWC

15. NUMBER OF PAGES

21

16. PRICE CODE

17. SECURITY CLASSIFICATION OF REPORT	18. SECURITY CLASSIFICATION OF THIS PAGE	19. SECURITY CLASSIFICATION OF ABSTRACT	20. LIMITATION OF ABSTRACT
Unclassified	Unclassified	Unclassified	